Dart-Leader and K-Leader Velocity From Initiation Site to Termination Time Resolved with 3D Interferometry

Daniel P. Jensen, Richard G. Sonnenfeld, Mark A. Stanley, Harald E. Edens, Caitano da Silva, Paul R. Krehbiel

Langmuir Laboratory for Atmospheric Research, at New Mexico Institute of Mining and Technology

Key Points:

- Two K leaders and three dart leaders were recorded on the same channel for one flash using a 3D Interferometer (3DINTF).
- Initial velocity generally increased with successive leaders on the same channel.
- Dart leader and K leader velocity consistently decreased with progress along the channel.

Corresponding author: Daniel Jensen, `djensen@alumni.nmt.edu`

Abstract

Simultaneous data from two interferometers separated by 16 km and synchronized within 100 ns was collected for a thunderstorm near Langmuir Lab on October 23, 2018. Analysis via triangulation followed by a least-squares fit to time of arrival across all six antennae produced a three-dimensional interferometer data set (3DINTF). Simultaneous Lightning Mapping Array (LMA) data enabled an independent calculation of 3DINTF accuracy, yielding a median location uncertainty of 200 m. This is the most accurate verified result to date for a two-station interferometer. The 3D data allowed profiling the velocity of multiple dart leaders and K leaders that followed the same channel. 3D velocities calculated from the in-cloud initiation site to ground ranged from 3×10^6 m/s to 20×10^6 m/s. Initial velocity generally increased with subsequent leaders, consistent with increased conditioning of the channel. Also, all leaders showed a factor of two to three decrease in velocity as they proceeded over 15 km of channel. We speculate that the velocity decrease is consistent with energy lost in the reionization of the leader tip. This paper includes an appendix providing details of the triangulation technique used.

1 Introduction

1.1 Brief History of VHF Instrumentation for Lightning Studies

Very High Frequency (VHF) radiation has been used to study lightning since the 1960's because of its ability to penetrate clouds, where most lightning activity occurs. This type of instrument was pioneered by Oetzel and Pierce (1969), who describe an instrument with three antennas $\sim$ 30 m apart arranged in a right triangle. Their design was narrowband but they suggested signal strengths should be sufficient for any band between 30 MHz and 100 MHz. This design bore a striking resemblance to modern interferometers (INTF), but it only measured the azimuthal direction to a flash. The early INTFs of Warwick et al. (1979), Hayenga (1984) and, Rhodes et al. (1994) used analog phase detection (mixers) due to limitations in digital technology. They operated in narrow frequency bands so that the intermediate frequency signal was within band of available signal processing electronics. These INTFs could measure both the azimuth and elevation of sources, but not the range to the source. Narrowband INTFs can improve their angular resolution by adding antennas on baselines of different lengths to allow the elimination of phase ambiguity (Rhodes et al., 1994; Shao & Krehbiel, 1996).

Beginning in the late 1990s, improvements in available digitizer speeds allowed the development of broadband digital INTFs with short ($\sim$ 1 μs) recording times that could be triggered multiply during a single flash (Shao et al., 1996; Kawasaki et al., 2000). These instruments took the Fourier transform of signals from multiple antennae to digitally recover the relative phase information. Broadband INTFs can use the higher frequencies in their data-stream to achieve the high angular resolution of a longer baseline narrowband INTF, while using the lower frequencies to remove the phase ambiguity of a narrowband INTF. Despite these advantages, the short recording lengths available for the first broadband INTFs made data interpretation challenging; each VHF event lost the "context" of the entire lightning flash.

More recently (Stock et al., 2014) developed a broadband digital INTF with long continuous recording times ($\sim$ 2 s) using cross-correlation to measure time delays between antennas. Long recording times enabled an entire flash to be captured without loss of context caused by gaps in the data set, while cross-correlation removed the "phase-wrap" problem by directly measuring the time-differences between antenna waveforms, making the INTF a short baseline TDOA system. This present study builds heavily on the instrumentation used in Stock et al. (2014) and Stock (2014). The station INTF01 in this study used similar active antennas (with some cost-reduction changes) and processing software, while the second INTF station (INTF02) used a modified antenna design and updated processing code based on the same principles as the earlier work.

Another common method of studying lightning through VHF emissions is with time of arrival (TOA) instruments, such as those developed by Proctor (1971), Poehler and Lennon (1979), and Rison et al. (1999). TOA instruments measure the arrival time of individual pulses at a number of different stations several kilometers apart, and use the TOA differences to determine the location of the source in 3D space. The Lightning Mapping Array (LMA) (Rison et al., 1999) is a widely used TOA instrument. With a sufficient number of stations and good line of sight the LMA is able to locate sources over the array to within 12 m_{RMS} horizontally and 30 m_{RMS} vertically (Thomas et al., 2004).

Three-dimensional lightning mapping has also been done with interferometry by combining angular measurements from two different stations. Mardiana et al. (2002) created a three-dimensional INTF (3DINTF) which they estimated to locate sources within 600 m, and Liu et al. (2018) estimated their 3DINTF was accurate within 500 m. These 3DINTFs used segmented recording rather than the continuous recording used in the present study. B. M. Hare et al. (2018) have also used a VHF radio telescope, the Low Frequency Array (LOFAR), to map lightning with accuracy on the order 1 m horizontally and 10 m vertically (B. Hare et al., 2020). 3D lightning mapping instruments exist at lower frequencies as well, notably the Huntsville Alabama Marx Meter Array (HAMMA) (Bitzer et al., 2013) operating at 1 Hz to 400 kHz, the Fast Antenna Lightning Mapping Array (FALMA) (Wu et al., 2018) operating at 500 Hz to 500 KHz, and the Position by Fast Antenna (PBFA) instruments of Stolzenburg, Marshall and Karunarathna et al. (2017).

1.2 New Contributions

In this paper we will go into some detail on the analysis procedure of one of the first continuous 3D interferometers (3DINTF) and verify its accuracy against a collocated LMA. We will also derive time and space-resolved velocity profiles of repeated K leaders and dart leaders and speculate on what they teach us about leader physics. It thus behooves us to also review what is known about dart and K Leaders.

1.3 Dart Leaders and K Leaders

1.3.1 Terminology

Dart Leaders are fast lightning leaders that retrace channels previously created by slower leaders in virgin air. Kitagawa (1957) coined the term K change (K for"Kleine", or small) to describe an electric field change signature which he suggested was caused by the same process as a dart leader. Leaders associated with K changes are often called K leaders or K-processes waves (Winn et al., 2011). Despite the recognized equivalence of the physics behind K leaders and dart leaders (Kitagawa, 1957; Shao et al., 1995), a distinction continues to be made in the lightning community with the general understanding that a dart leader progresses to ground while a K leader remains in the clouds. This distinction is somewhat blurred by authors who refer to failed or attempted dart leaders which do not reach the ground (Shao et al., 1995; Rhodes et al., 1994). It seems clear that there should be a common name which encompasses all such events if the physics behind them is believed to be the same. In search of a common name some authors refer to all such activity as recoil leaders/streamers (Akita et al., 2010; Mazur, 2016), or retrograde leaders (H. E. Edens et al., 2012). We suggest to make the term dart leader encompass all leaders of this type, since it was the first term used to describe this phenomenon, it is descriptive of their high velocity, it is agnostic of the detailed physical mechanism which is not yet well established, and it can be inclusive of both retrograde leaders on positive channels as described by H. E. Edens et al. (2012), or prograde leaders on negative channels as observed by Shao et al. (1995). (K leaders could perhaps be called IC dart leaders if it is necessary to specify that they are not followed by a return stroke.) However, until the community reaches a new consensus, we will use existing terminology. In this paper, we analyze two K leaders followed by three dart leaders; all using parts of the same channel.

1.3.2 Properties of Dart Leaders and K Leaders

Dart leaders were identified as early as the 1930's by Schonland et al. (1935) using a Boys camera, where two dimensional average velocities were found to range from 1×10^6 m/s to 23×10^6 m/s , an order of magnitude or two higher than initial leaders. Further studies of dart leaders are rather consistent with these velocities. Table 1.3.2 shows dart leader velocity reported in selected papers, along with some K leader velocities, which fall in the same range. Schonland et al. (1935) also reported that slower dart leaders corresponded with longer intervals between return strokes. This observation was corroborated also by Loeb (1966) and Shao et al. (1995), and in laboratory analogues (Winn, 1965).

Paper	Average Velocities (m/s)	leader type
(Schonland et al., 1935)	1×10^6 to 23×10^6	Dart
(Loeb, 1966)	2×10^6 to 20×10^6	Dart
(Jordan et al., 1992)	6×10^6 to 50×10^6	Dart
(Shao et al., 1995)	1×10^6 to 10×10^6	Dart
(Stock et al., 2014)	3×10^6 to 17×10^6	K leader
This study	2×10^6 to 20×10^6	Dart & K

Table 1. The range of average dart (and K) leader velocities reported by selected studies.

Laboratory analogues of dart leaders also exhibited an effect of the ionization waves slowing down as they propagated along the channel (Winn, 1965). Jordan et al. (1992) used a streaking camera to study triggered lightning in New Mexico and Florida. They calculated average velocity of two short segments of the observed channel and found that New Mexico dart leaders tended to slow down as they approached ground. For triggered lightning in Florida they found, on average, a higher measured velocity for dart leaders in the final $\sim$ 250 m approaching the ground. Stock et al. (2014) used LMA data to interpolate 3D locations from 2D INTF sources. It was observed, on average, that K leaders accelerated briefly after initiation and decelerated as they progressed down their channels.

Rakov (1998) modeled dart leaders propagating on transmission lines. At an estimated temperature of 3000 K, Rakov found that the conductivity of the decayed channel is too low to allow for the propagation of a dart leader. This suggests to us that the transmission line model is incomplete and that energy must be pumped into the leader tip. Re-ionization of the decayed channel is a necessary condition for dart leader propagation, and the rate of ionization should be related to the propagation speed.

2 Methods

2.1 3D Interferometry

This study used two INTF stations separated by 16 km, each with three antennas with roughly 25 m baselines. The first station (INTF01) was located at a site designated West Knoll at Langmuir Laboratory. The second station (INTF02) was located at the airport in Magdalena, New Mexico. INTF01 sampled at 180 MS/s, while INTF02 sampled at 360 MS/s, and both were band limited to 20–80 MHz before processing. INTF02 was time synchronized by GPS, and INTF01 was synchronized by comparing arrival times with a GPS-synchronized LMA as described in more detail in section 2.2.2.

Raw data was first processed separately using three antennas at each station to calculate azimuth and elevation angles according to the methods outlined in (Stock et al., 2014) and (Stock, 2014). Cross-correlation is used to measure the time of arrival difference between each pair of antennas. The time of arrival difference between any two antennas determines the source angle as

$$\cos \alpha = \frac{c\tau_d}{d} \tag{1}$$

where α is the incident angle relative to the baselines between the two antennas, c is the speed of light, τ_d is the difference in time of arrival, and d is the distance between the two antennas. For a set of three antennas arranged in a triangle independent angles α and β can be calculated. These uniquely give the direction to a source, but not its range. From α and β azimuth and elevation may be readily calculated.

Azimuth and elevation angles from two different INTF stations can be combined using the triangulation method as detailed by Thyer (1962) and Liu et al. (2018). A similar method was used by Mardiana et al. (2002). The triangulation algorithm, along with additional details for different station configurations, are included in Appendix A. The triangulation method gives a 3D location for a source given an azimuth and elevation angle measured from two different locations. In any two station method, there is an additional challenge in determining which sources on each station have a correspondence. In the analysis presented here, we found a correspondence for about half of the detected sources at station 1 (station 2 operated at a higher frequency so it was able to detect about twice as many sources).

For a source detected by the two stations the maximum possible time difference is determined by

$$T = D/c \tag{2}$$

where D is the distance between stations and c is the speed of light. For the two INTF stations used, separated by 16 km, that time is 53 μs. We achieved source matching between the stations by calculating the triangulated locations for every possible pair of sources between the two stations that are separated by 53 μs or less. The source time corresponding to each trial location was calculated using

$$t_0 = t_1 - \frac{\sqrt{(x_0 - x_1)^2 + (y_0 - y_1)^2 + (z_0 - z_1)^2}}{c} \tag{3}$$

where t_0, x_0, y_0, and z_0 are the source time and x, y, and z coordinates respectively for the trial location, and t_1, x_1, y_1, and z_1 are the time of arrival and x, y, and z coordinates respectively for one of the antennas (the choice is arbitrary), and c is the speed of light.

We then determined the best match by calculating a goodness-of-fit parameter,

$$\chi^2 = \sum_{i=1}^{N} (t_i^{obs} - t_i^{fit})^2 \tag{4}$$

where t_i^{obs} is the observed time of arrival at the i-th antenna, t_i^{fit} is the time of arrival corresponding to the trial location, and N is the number of antennas. The trial location that gave the lowest χ^2 value was chosen as the best match location. Best matches were first identified for every source from INTF01, so that each source from INTF01 was matched to only one source from INTF02. Best matches were then determined for every INTF02 source that was chosen as a best match for at least one INTF01 source, so that no source from either station would be included in more than one match in the final set.

We then further refined the 3D locations by using a minimization algorithm to calculate the source location corresponding to the minimum χ^2 value as given by equation 4, similar to the method described in Thomas et al. (2004, 2000) for the LMA. The Gauss-Newton algorithm was used because it was simpler to implement for this new application, though the Levenberg-Marquardt algorithm used by Thomas et al. may have more ideal convergence behavior.

2.2 3DINTF Validation

2.2.1 Time correction on INTF01

INTF01 data was synchronized with network time, which provided an accuracy of roughly $\sigma = \pm 4$ ms, however 3DINTF requires timing accuracy of order 100 ns is needed. A high-precision GPS attached to one of the digitizer channels of the INTF could provide such accuracy, but none was present for this study. Fortunately, through a synchronization of INTF pulse and LMA pulse arrival times, INTF time can be corrected using the LMA as a reference. This same procedure also results in a set of points which can be used to check the accuracy of the 3DINTF. Details of this synchronization scheme will be discussed in section 2.2.2.

2.2.2 INTF to LMA correlation

To verify the validity of the 3DINTF locations and estimate location accuracy we 3DINTF and LMA sources for a set of four flashes. Matching of LMA and INTF data was carried out as follows:

The LMA data used had already been processed by well-established code which turns time-stamped VHF pulses into located data points that are time-stamped with the time of emission at the source location. Since the goal of LMA/INTF correlation is to locate INTF points at which initially only a time of a arrival at an INTF antenna is known, the LMA source times are updated to the times at which each source would arrive at the selected INTF antenna.

Raw VHF data from the selected single INTF antenna was processed with a 60-66 MHz forward-backward (zero-phase) Butterworth filter of net order N=2. (The *scipy.signal.butter* function was used). The filtered INTF signal is now analogous to the raw LMA receiver data. A Hilbert transform was next applied to produce a power envelope. The largest peak power in a fixed window is then recorded along with its time stamp. Since the LMA only records peak powers in fixed windows, the INTF and LMA peaks are assumed to correspond to the same source. This is true often enough for the technique to work. The pairwise time difference between all INTF VHF peaks and all LMA arrival times is plotted in a histogram with one microsecond bins. An initial time offset estimate is determined by taking a weighted average of the histogram peak and neighboring bins. Once the first time offset is calculated, a linear regression between LMA and INTF source times is calculated to produce a refined time offset.

Having corrected INTF time with the previous processing step, the strongest INTF pulse in a 40 μs window is determined and a time match to an LMA source

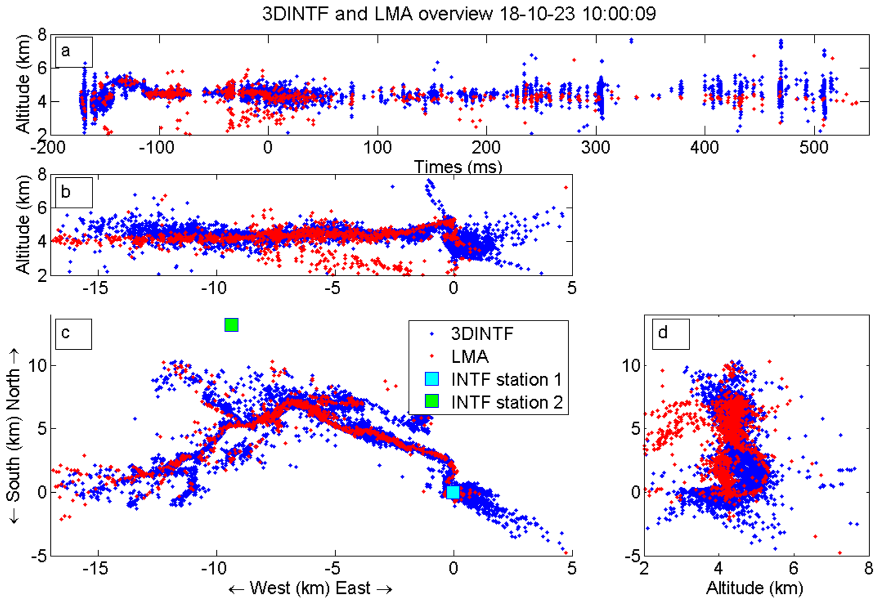

Figure 1. Comparison of 3DINTF and LMA for the 10:00:09 flash on October 23rd, 2018. Plots show altitude vs time **(a)**, altitude vs east/west **(b)**, north/south vs east/west **(c)**, and north/south vs altitude **(d)**. 3DINTF sources are marked in blue and LMA sources are in red.

within one microsecond is sought. Matches are added to the pulse-pair list. Once a pulse-pair list is available, it is filtered to keep only the pairs which were also 3D located by the INTF. The LMA locations on this filtered list can now be directly compared against the 3DINTF locations. The result are Figures 1 and 2.

2.2.3 Determining Accuracy of 3DINTF

In the procedure described above the LMA was used initially only to correct the station time on INTF01. Fundamentally, the LMA measurement and the 3DINTF measurements are independent. Thus the matched INTF/LMA pulse pairs derived as per section 2.2.2 can be used to verify the accuracy of the 3DINTF method. Figure 1 illustrates the good agreement between the LMA locations (red) and the independently calculated INTF locations (blue) for the flash to be analyzed in this paper. Overall the distances between matching 3DINTF and LMA points were roughly log-normally distributed, with a median error of about 200 m. Histograms of the discrepancy in each coordinate direction and the overall discrepancy between the 3DINTF and the LMA are shown in Figure 2. The median discrepancy is reported rather than an RMS value because the median is not distorted by the long tails, which may be at least partly caused by bad matches between the data sets. The LMA only had 8 stations operating, with many sources only located by 6 or 7 stations, and the storm was on the outside edge of the array, so we estimate that the LMA also had errors on the order of 100-200 m for these flashes. An LMA with 13 or more stations can have RMS errors as low as 20-30 m for sources over the array (Thomas et al., 2004). The small number of LMA stations in operation and uncertainty in matching between the 3DINTF and LMA means the measured discrepancies only serve as an upper bound on the uncertainty in the 3DINTF source locations, the true median accuracy may be better than 200 m. We plan to conduct a more precise measurement of 3DINTF accuracy in the future.

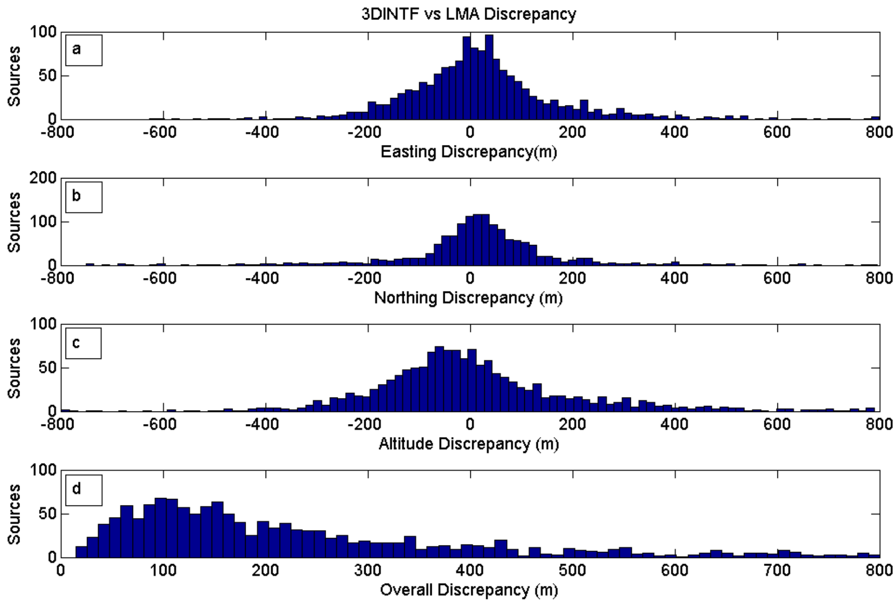

Figure 2. Histograms of the measured discrepancies between matching 3DINTF and LMA source locations, east-west discrepancies **(a)**, north-south discrepancies **(b)**, altitude discrepancies **(c)**, and overall 3D discrepancies **(d)**.

2.3 Velocity Estimation

The set of sources in the dart/K leaders displayed a change in position that was generally monotonic in time and there was little VHF activity on other channels during their occurrence. This allowed a simple rolling average (boxcar window) to be used to filter that leader's position vs. time. The values for each coordinate were calculated as:

$$\overline{x}_1(i) = \frac{1}{N} \sum_{k=i}^{i+N} x(k) \tag{5}$$

where N is the number of points averaged over, $x(k)$ is the k-th data point in the set of x coordinates for sources in the leader, and $\overline{x}_1(i)$ is defined as the x-coordinate for the i-th point in the leader, $\overline{x}$ being a traditional way to denote the average. The y, z, and time coordinates of the leader were smoothed in the same way. In order to estimate the velocity these coordinates were compared to the next N points, with coordinates defined as $\overline{x}_2(i) = \overline{x}_1(i + N)$ and the velocity was calculated as

$$v_1(i) = \frac{\sqrt{(\overline{x}_2(i) - \overline{x}_1(i))^2 + (\overline{y}_2(i) - \overline{y}_1(i))^2 + (\overline{z}_2(i) - \overline{z}_1(i))^2}}{\overline{t}_2(i) - \overline{t}_1(i)} \tag{6}$$

Several different values N were tested. $N = 40$ was found to be a good balance between channel tracking and noise rejection. Figure 3 shows how averaging over a smaller number of points on the second dart leader better follows the exact path of the channel while Figure 4 shows that averaging over a small number of points yields an excessively noisy velocity plot. Comparing these rolling averages also serves as an estimate in the uncertainty of our calculated velocities. The $N = 40$ and $N = 10$ velocities have an RMS difference of 5×10^6 m/s, while the $N = 40$ and $N = 100$ velocities have an RMS difference of 2×10^6 m/s. If we assume the dart leader propagates monotonically, the

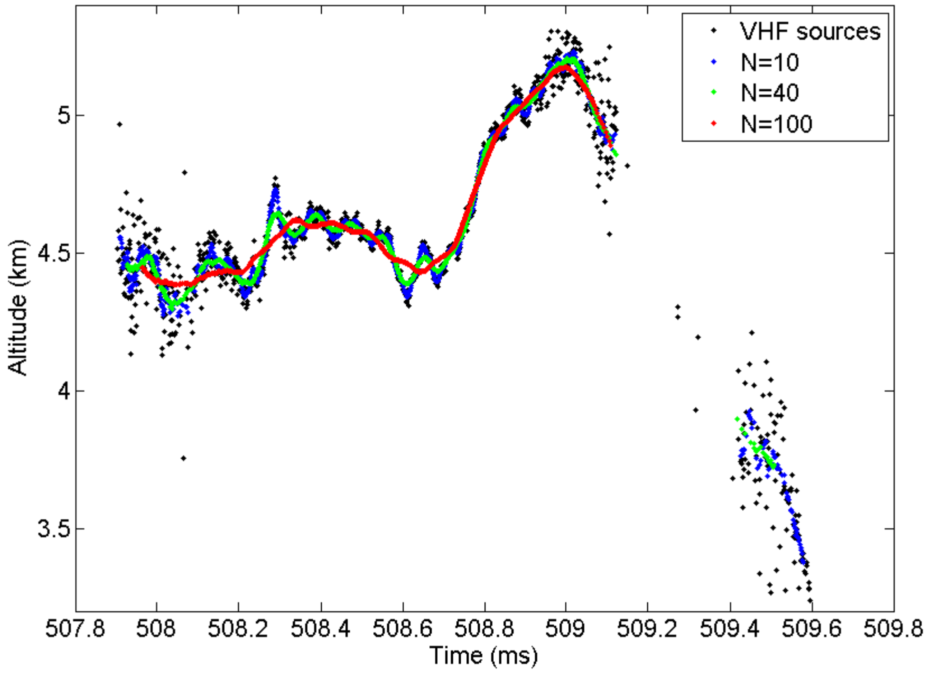

Figure 3. Comparison of rolling averages of the second dart leader using different numbers of points, in plots of altitude vs time, with the original VHF sources (black) and the rolling average points. Averages are performed using 10 points (blue), 40 points (green), and 100 points (red). The gap in data is caused by a null in sensitivity directly over the INTF01.

uncertainty is likely closer to the lower value. Averaging for $N = 10$ gives sharp jumps in position/velocity due to uncertainty in the individual source locations.

3 Results

3.1 Charge Region Identification

Figure 5 shows charge regions identified by the LMA for flashes happening near Langmuir Lab between 09:50:00 and 10:20:00 UTC on 2018-10-23. Charge regions were identified following the procedure outlined by Hamlin et al. (2003). The plot shows the tripolar structure typical of many thunderstorms, as described by Williams (1989) and Marshall et al. (2005). The lower positive region appears to be around 2.5-3.5 km MSL, the main negative region appears to extend from roughly 4 km to 6 km, and the upper positive region is spread from 6 km to 9 km MSL. The altitudes of these regions are significantly lower than those observed by Marshall et al. (2005) and H. E. Edens et al. (2012), but this is to be expected as their observations were made in July and August, and this paper discusses results from a storm in late October. The charge regions are known to be defined by temperature rather than altitude (Krehbiel, 1986), and with lower temperatures at the ground in late October we would expect the charge regions to be lower in altitude.

There is no reason 3DINTF data couldn't be used to perform a similar charge analysis in the future, but the data is not currently compatible with the existing tools for the LMA. Figure 6 shows a histogram of the altitudes of 3DINTF sources from

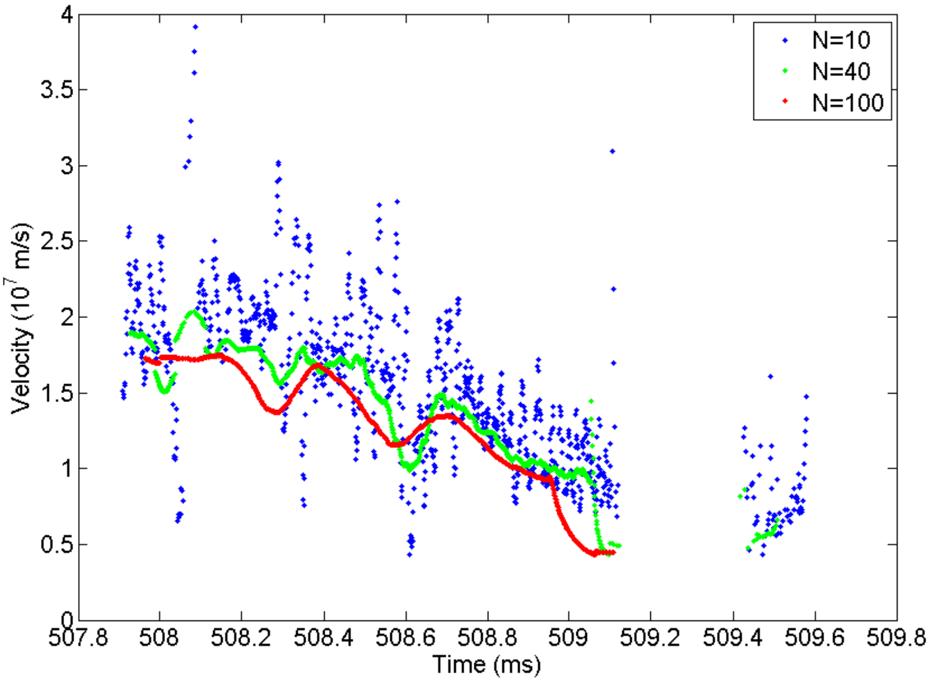

Figure 4. Comparison of different sized rolling averages of the second dart leader on the plots of velocity vs time. Averages are performed using 10 points (blue), 40 points (green), and 100 points (red). The gap in data is caused by a null in sensitivity directly over the INTF01.

10:00:00 UTC to 10:20:00 UTC. The upper positive (6 km to 9 km MSL) and main negative (4 km to 6 km MSL) charge regions identified by the LMA are also visible in the 3DINTF data, and their rough extent can be identified from the histogram alone, assuming the storm has a normal tripolar structure. The lower positive region is not obviously present in the 3DINTF histogram, but we have only processed 4 flashes for the 3DINTF in this time period, while Figure 5 was compiled from 11 flashes where the charge structure could be easily identified. (There were 43 flashes in all in this time period.) It is reasonable to suppose the 3DINTF histogram would be closer to the charge structure identified by the LMA if more flashes were included from the chosen interval. The LMA and individual INTF stations did detect a similar number of flashes, but since this was the first test of a new instrument configuration and a new processing technique only a few flashes were processed. The LMA data for Figure 5 was processed with 80 μ s windows and limited to at least seven participating stations for each source. The data set consists of just under 18,000 sources between the 43 flashes. The 3DINTF, by contrast, captured over 172,000 sources between just the 4 processed flashes.

3.2 Flash Overview

In all the plots that follow, the origin of the coordinate system (X=0, Y=0) is located at station INTF01. The INTF02 station was located 13 km north and 9 km west from the INTF01. The measurements were performed in mountainous terrain. The altitude of the two interferometers is 3.16 km and 2.05 km respectively.

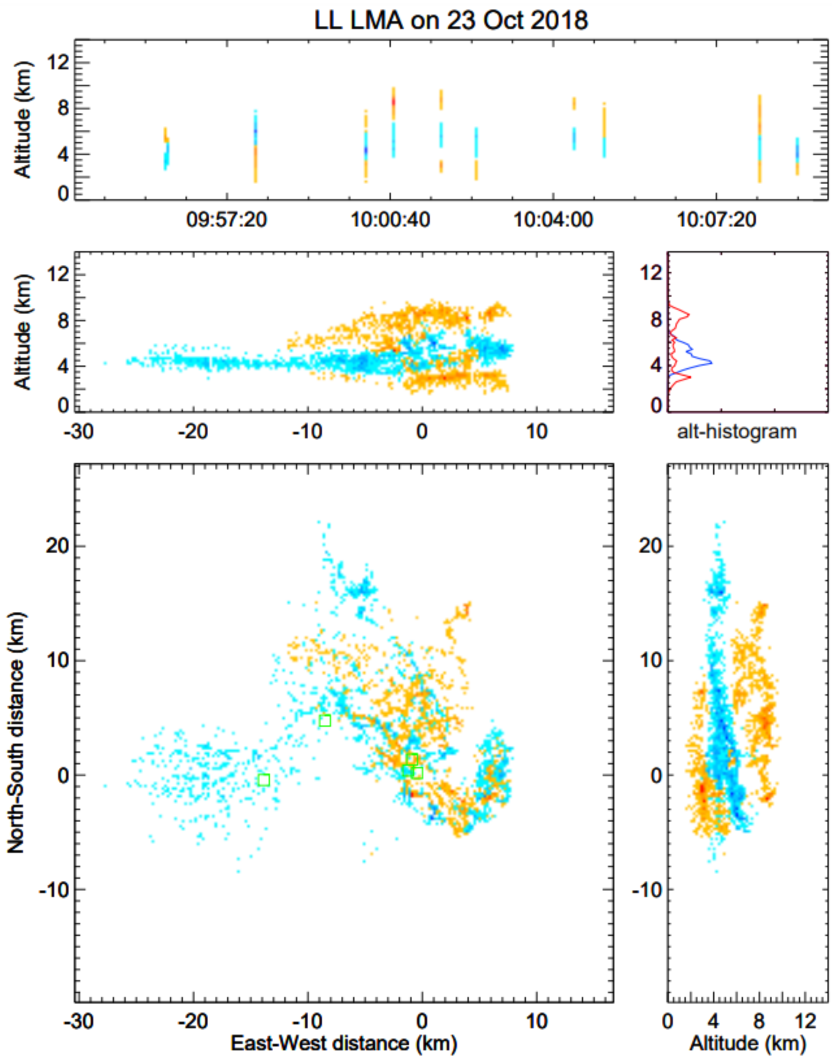

Figure 5. Charge structure as identified by the LMA for flashes happening between 09:50:00 UTC and 10:20:00 UTC near Langmuir Lab on 2018-10-23. Negative charge is shown as blue, positive as orange/red.

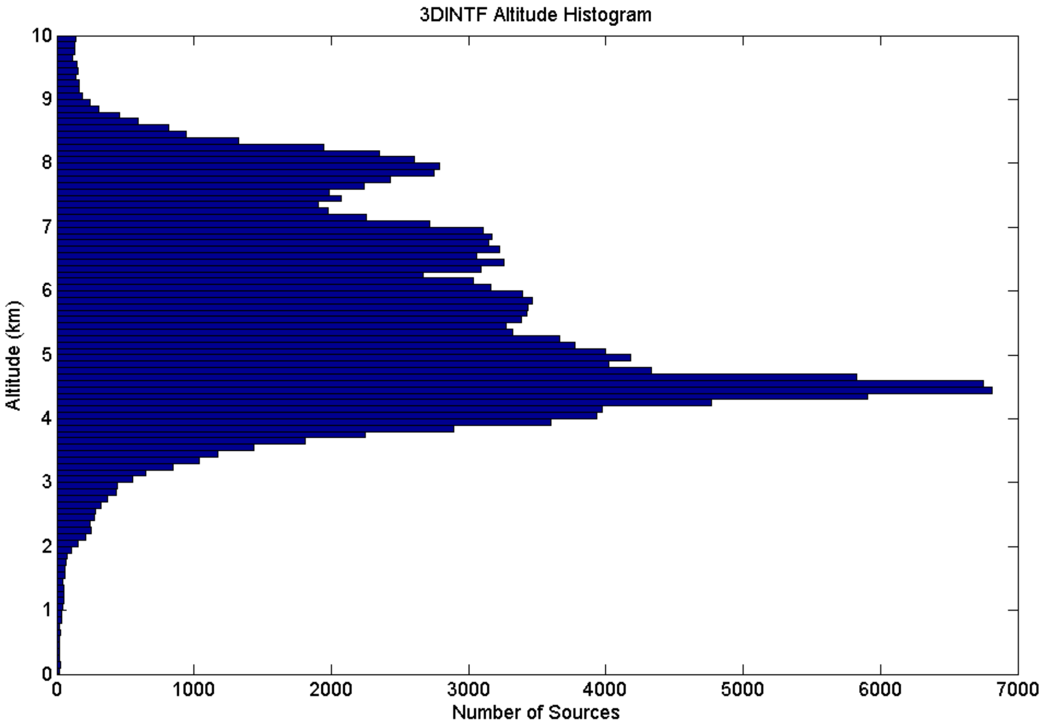

Figure 6. A histogram of 3DINTF VHF source altitudes for flashes happening between 10:00:00 UTC and 10:20:00 UTC near Langmuir Lab on 2018-10-23

Figure 7 gives an overview of the entire lightning flash of interest. The data is presented in the style of an LMA Plot, which has become a familiar way of displaying three-dimensional data (Thomas et al., 2004). As described in section 2.2.2, an LMA was used to check the validity of the 3DINTF mapping, but all the 3D locations shown here are solely INTF results. Other than the storm overview in Figure 15, no further data obtained from the LMA is presented in this paper.

We first present an overview to orient the reader, and then return to discuss the flash in more detail stroke by stroke. (For a more complete picture of the flash development please refer to the animation included in the supplementary material (Jensen et al., 2020).) The flash begins with two cloud-to-ground (CG) strokes, visible as nearly vertical features in 7a (before -150 ms, colored dark blue). The National Lightning Detection Network (NLDN) (Cummins et al., 1998) also identifies negative CGs at this time (indicated by diamonds in the plots). The negative charge brought to ground in the initial -CGs results in a pocket of reduced negative charge in the region above the CG grounding locations. It is thus energetically favorable for a positive leader to issue horizontally from this reduced negative charge into the main negative charge, and this is precisely what is shown in the blue/yellow/red data points that move west from the origin in panel "b". (Many of these points are covered by the brick red points of dart leaders that occur later in the flash). Once this positive leader has reached a point roughly seven km west of the origin, a negative K leader travels back along the horizontal channel. (This K leader begins around t=-40 ms, and should be coloured blue, but is likewise buried beneath the brick red data points from later dart leaders.) The positive leader resumes its extension with blue through green data points, and there is another negative K leader at t=230 ms. Positive leader growth then

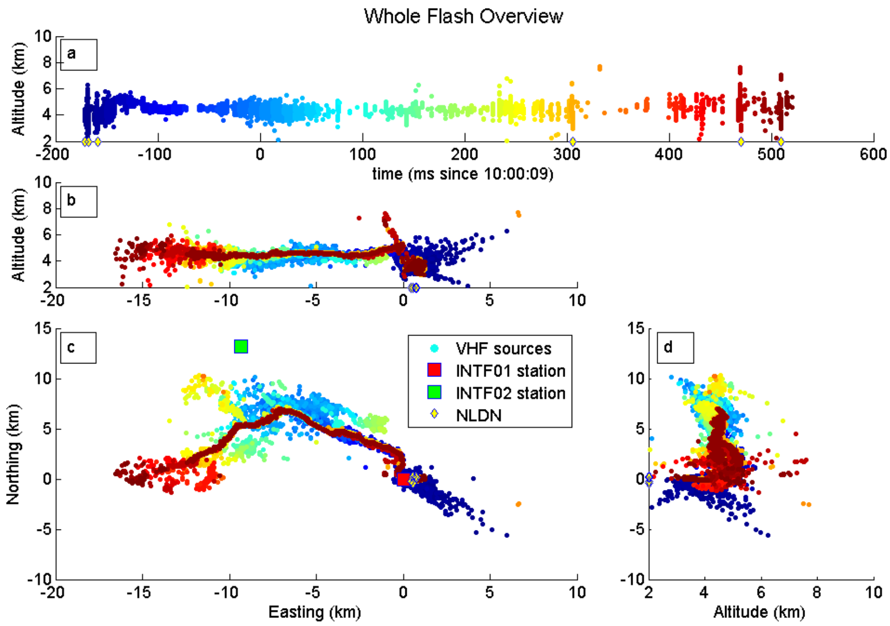

Figure 7. Overview of the entire flash from 10:00:09 UTC on 2018-10-23, with sources colored blue to red according to time. **(a)** altitude vs time, **(b)** altitude vs. east/west position, **(c)** Plan view (north/south vs. east/west), **(d)** altitude vs. north/south position. The 3DINTF VHF sources are shown along with the location of the INTF01 and INTF02 stations, and the time and location of NLDN strokes. (In panel c, the NLDN ground-strike points are immediately to the east of INTF01)

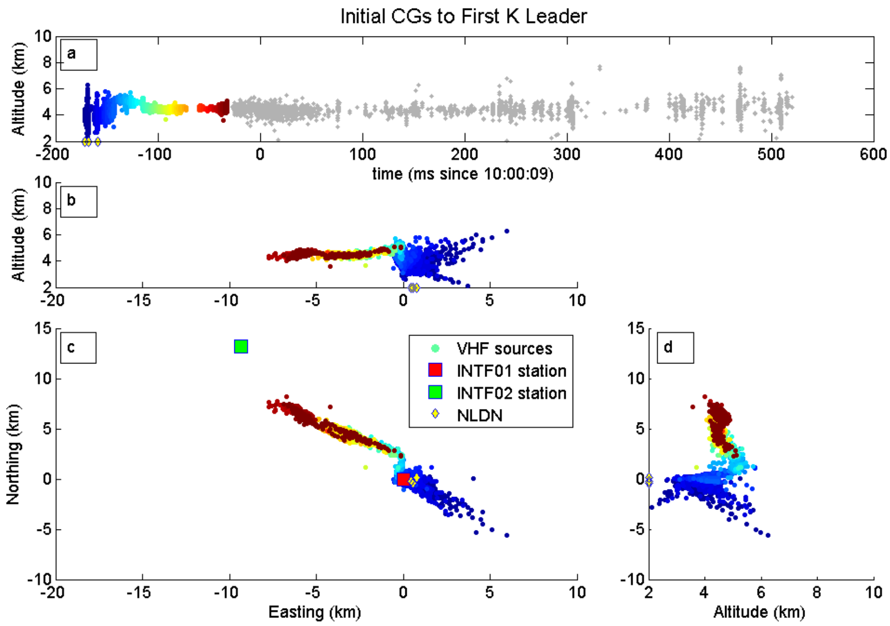

Figure 8. The beginning of the flash up to the first K leader. Sources colored blue to red according to time.**(a)** altitude vs time,**(b)** altitude vs. east/west position, **(c)** Plan view (north/south vs. east/west), **(d)** altitude vs. north/south position. The 3DINTF VHF sources are shown along with the location of the INTF01 and INTF02 stations, and the time and location of NLDN strokes (yellow diamonds).

continues with the yellow and orange points until the first dart leader occurs around t=310 ms. After the first dart leader, the positive leader continues to grow, leading to a second dart leader at 470 ms, and a third one at 510 ms. Having understood the big picture, let us look at each of these sections in more detail.

3.2.1 K Leaders

Figure 8 shows the development of the flash up to the first K leader, with sources colored by time. After the two initial negative CGs near the origin the positive leader propagates primarily to the northwest (in panel c). This positive leader appears to remain in a single well defined channel until about -40 ms, when the first K leader begins. (The K-leader is shown in brick red in Figure 8b,c,d.)

After the first K leader the positive leader resumes propagation, and begins blooming into many branches as seen in Figure 9. There are clear large branches to the north-west, east, and south-west, as best seen in Figure 9c. The branch to the north-west develops into the second K leader, which reaches roughly the same point along the channel as the first K leader. Again, the K-leader shows up as a well-defined channel of brick red points within the more scattered branches of the positive leader.

3.2.2 Dart Leaders

Figure 10 shows continued blooming in the north-west and south-west branches of the positive leader, leading to the first dart leader just after 300 ms. The NLDN

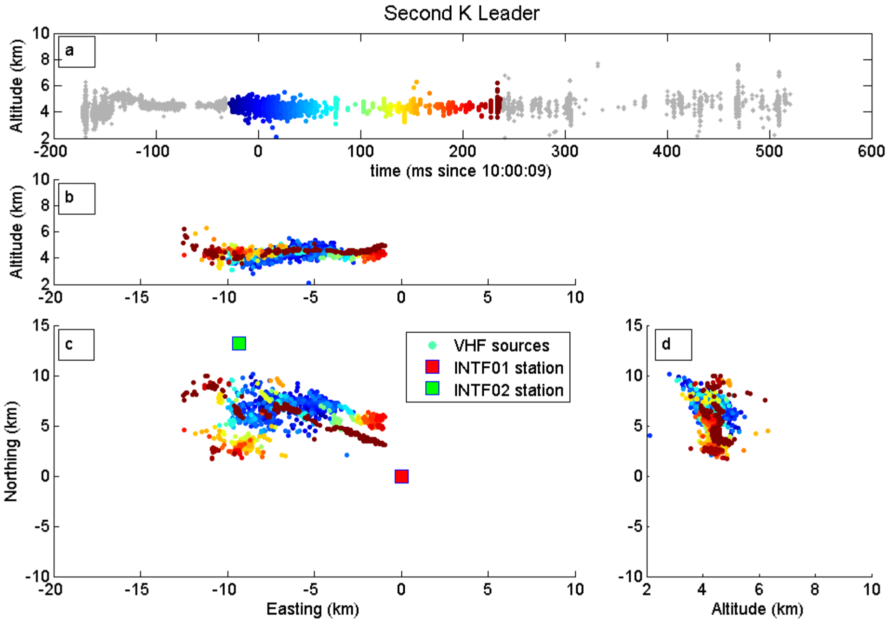

Figure 9. Overview of the second K leader and leader growth that precedes it. Sources colored blue to red according to time. **(a)** altitude vs time, **(b)** altitude vs. east/west position, **(c)** Plan view (north/south vs. east/west), **(d)** altitude vs. north/south position. The 3DINTF VHF sources are shown along with the location of the INTF01 and INTF02 stations.

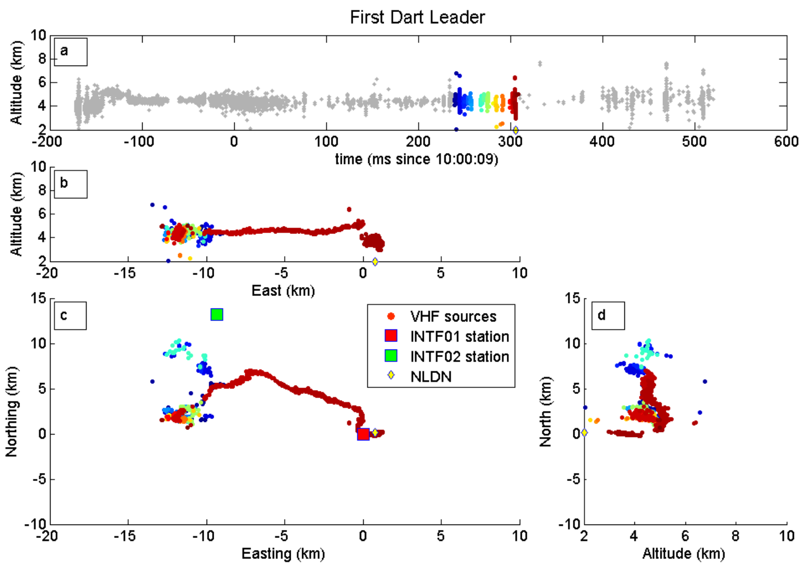

Figure 10. Overview of the first dart leader and the blooming that precedes it, with sources colored blue to red according to time. **(a)** altitude vs time, **(b)** altitude vs. east/west position, **(c)** Plan view (north/south vs. east/west), **(d)** altitude vs. north/south position. The 3DINTF VHF sources are shown along with the location of the INTF01 and INTF02 stations, and the time and location of NLDN strokes.

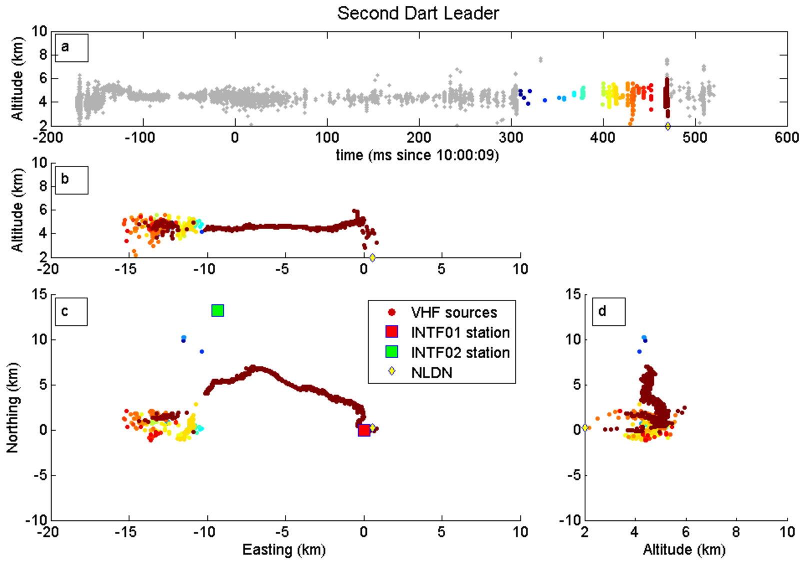

Figure 11. Overview of the second dart leader and the blooming that precedes it, with sources colored blue to red according to time. **(a)** altitude vs time,**(b)** altitude vs. east/west position, **(c)** Plan view (north/south vs. east/west), **(d)** altitude vs. north/south position. The 3DINTF VHF sources are shown along with the location of the INTF01 and INTF02 stations, and the time and location of NLDN strokes.

identifies this dart leader as a negative CG, which is consistent with it being a negative leader propagating back down a channel initially created by positive breakdown.

Figure 11 shows further blooming of the positive leader, primarily in the south-west branch, which leads to a second dart leader around 470 ms, again identified as a negative CG by the NLDN.

Figure 12 shows further positive leader growth in the south-west branch, and the third dart leader around 510 ms, following quite quickly after the second dart leader at 470 ms. This dart leader is again identified as a negative CG by the NLDN.

3.3 Reduced “branching” of dart leaders and K leaders

Having discussed the flash in detail, a feature of the data in Figure 7 and the subsequent dart and K leader figures should be remarked upon. Back at Figure 7, panels b and c clearly show a brick-red dart leader (the final one) overlaying the earlier positive leader points. In fact, that final dart leader overlays the earlier ones so completely that they cannot be seen. This fact will be useful in our forthcoming velocity calculations, but is itself of note. The great deal of “scatter” or “blooming” visible on all the VHF sources preceding the dart leaders is *not* a result of poor location precision. Rather, it seems to be characteristic of the much more highly branched nature of stepped leaders on the 100-1000 m scale as compared to dart leaders. Such small branches near the leader tip were observed by Ding et al. (2020) for negative leaders. Here we see them on a positive initial leader. (We do not claim to resolve any structure within the scattered initial leader sources.) This phenomenon has long been noted with video observations of dart leaders proceeding to ground. We want to clarify that it is *also* characteristic of the in-cloud portion of dart leaders, as well as K leaders. We suggest that this reduced branching tells us something about the physics

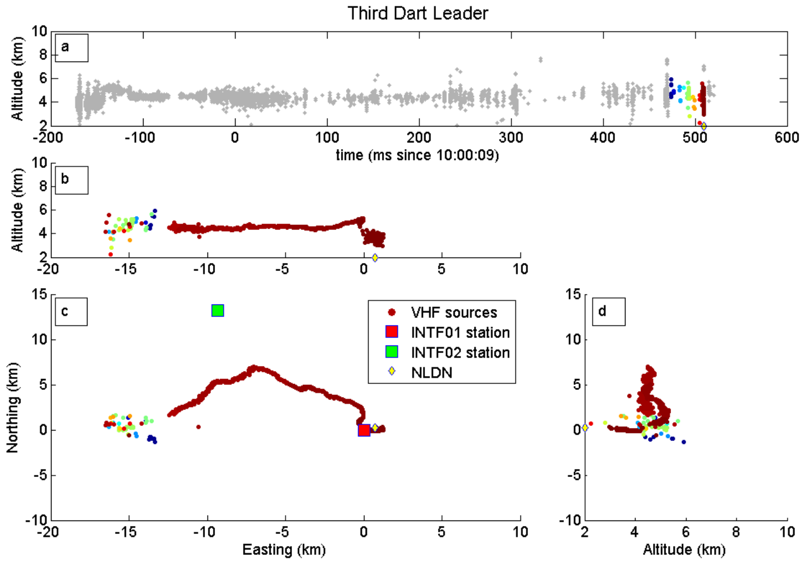

Figure 12. Overview of the third dart leader and the blooming that precedes it, with sources colored blue to red according to time. **(a)** altitude vs time,**(b)** altitude vs. east/west position, **(c)** Plan view (north/south vs. east/west), **(d)** altitude vs. north/south position. The 3DINTF VHF sources are shown along with the location of the INTF01 and INTF02 stations, and the time and location of NLDN strokes.

of a dart leader and that it is somehow a preferred path for the re-ionization wave. Similar observations were reported by Shao et al. (1995).

3.4 Velocity

Velocities for both K leaders and all three dart leaders are shown in Figure 13, while Figure 14 shows how the channel segments were aligned. The velocity of each dart or K leader was integrated over time to give a distance along the channel at each point, and the initial offsets of these integrated distances were adjusted so that the shared portions of each dart leader channel would align in the original spatial coordinates (altitude, northing, and easting), as shown in Figure 14. The zero point was arbitrarily chosen to be the beginning of the final dart leader. Figure 14 demonstrates that, for most of their length, all the K leaders and dart leaders share the same three-dimensional path. The leaders were aligned in this way in order to show how the velocity at each point along the channel varied between the K leaders and dart leaders. Some obvious trends appear, most notably the large dip in velocity around 7 km, which occurs in every dart and K leader that passed that point. The second K leader, which is already traveling slowly as it passes the location of the dip, is the only exception to this behavior. A smaller dip is also apparent in all three dart leaders at around 6.5 km (Figure 13). While we do not understand what is special about the locations of the speed dips, it seems that there is some reproducible feature (presumably related to overall charge structure of the storm) which causes the dips to occur repeatedly at the same location in the thundercloud.

The calculated velocities range from 2×10^6 m/s to 20×10^6 m/s. This agrees very well with the range of velocities other researchers have reported, as listed in Table 1.3.2. With the exception of the first K leader, which started very quickly and then dropped

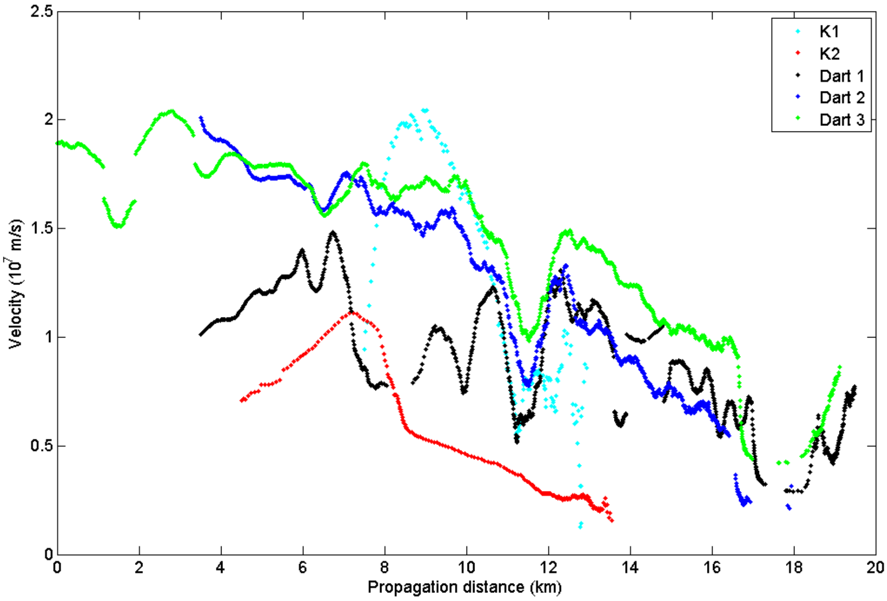

Figure 13. Plot of velocity versus distance propagated along the channel for all of the dart leaders and K leaders. Showing K leader 1 (cyan), K leader 2 (red), dart leader 1 (black), dart leader 2 (blue), and dart leader 3 (green). Zero propagation distance is arbitrarily set to be the start of the last dart leader.

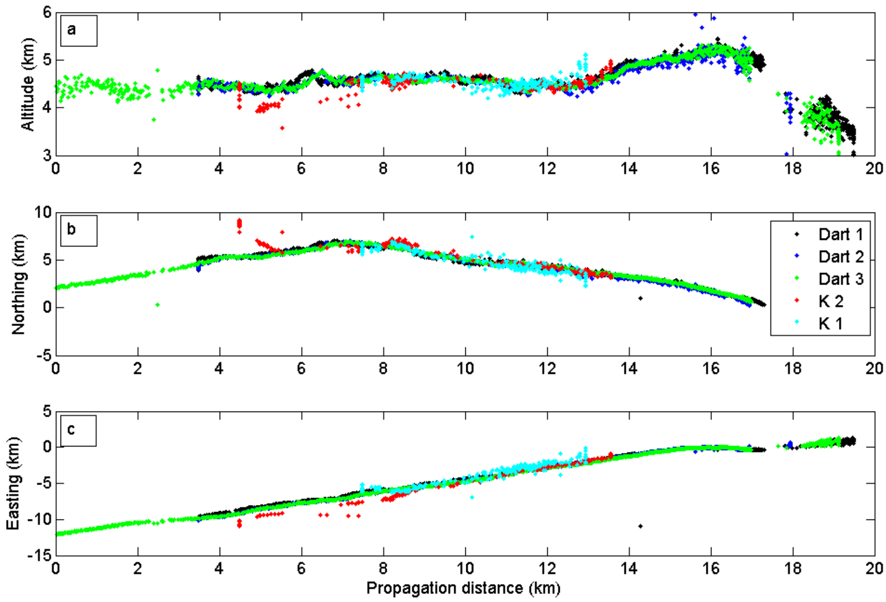

Figure 14. Plot showing how the channel segments were aligned for each dart leader and K leader. Showing K leader 1 (cyan), K leader 2 (red), dart leader 1 (black), dart leader 2 (blue), and dart leader 3 (green). Zero propagation distance is arbitrarily set to be the start of the final dart leader.

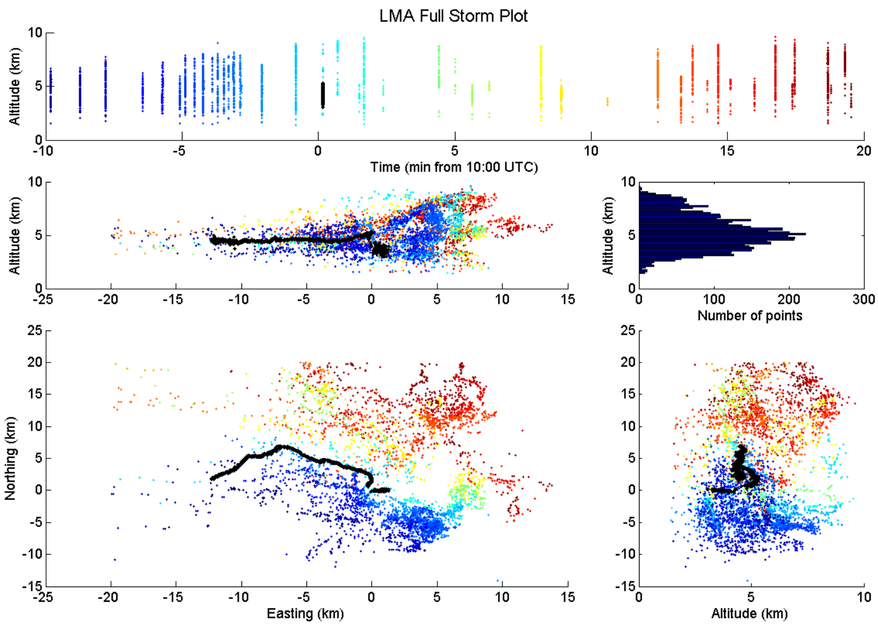

Figure 15. A plot of all LMA data from 2018-10-23 between 09:50 and 10:20 UTC, with flashes colored by time. The path of the dart leaders in the 10:00:09 flash is overlaid in black.

off again, the other 4 leaders generally increased in velocity with each subsequent pass along the channel. This is consistent with the channel being increasingly conditioned by previous leaders and return strokes (Behnke et al., 2005), although the first K leader shows that there must be multiple factors that determine the velocity of dart leaders and K leaders. Bazelyan and Raizer (1997) hints at a possible mechanism for conditioning in equation 2.17 and his statement that negative Oxygen ions require only 0.5 eV for reionization. Our data provide more clear examples of this poorly understood phenomenon.

3.5 Why does leader velocity decrease along the channel?

Figure 13 clearly shows velocity decreasing as the leaders progress along the channel, similar to the behavior Behnke et al. (2005) saw in initial leaders, but now in the context of dart and K leaders. We can think of three mechanisms which could lead to the observed velocity decreases. The first is increasing pressure as the leader propagates toward ground. Based on mean-free-path considerations, the leader might be expected to slow because of increased pressure. However there are two reasons to reject the pressure/speed hypothesis. First, it was previously shown that for negative stepped leaders descending from 10 km to ground the step length decreased with altitude, but the average velocity did not decrease. (The step rate increased inversely with the step length)(H. Edens et al., 2014). The second reason to reject the pressure/speed hypothesis is that roughly the first 10 km of channel progresses at a relatively constant 4.5 km of altitude (Figure 14a), while the next 5 km increases in altitude to 5 km. Thus, if there is any pressure effect on speed, we might expect a speed-up, contrary to observation. This suggests that pressure is not the driver of leader speed change for most of the leader.

The second explanation for speed change along the channel would be a change in local macroscopic field. It would be very exciting to have 3D interferometry in concert with quantitative background field mapping of the thunderstorm – but this falls under the realm of future work. We can only take an educated guess of where local fields might be high based on the LMA data for the storm. Figure 15 provides LMA data for the 20 minute period surrounding the flash of interest. We have overlaid the path of the dart leaders on top of the LMA data points in black. Figure 15 demonstrates that the dart leaders and K leaders progress from the western extremities of the storm into a region of much higher concentration of VHF sources in the east. The eastern region of the storm also piles VHF sources to a substantially higher altitude (see panel b). Absent other data, we would think that the updraft engine is operating fiercely right around zero kilometer E–W and that the ambient fields might be higher in this region. We would naively expect leaders to speed up as they entered higher ambient fields. To the extent that our extrapolations are correct, this second hypothesis for speed change of the leader fails as well.

What remains with highest probability is the third explanation; in which we consider a dart leader as a guided nonlinear ionization wave in a decaying plasma channel (See Bazelyan and Raizer (2000), Section 4.8). In this framework, the dart leader speed is proportional to the magnitude of the electric field created at the leading crest of this soliton. This high electric field is needed to reionize the decaying channel. As energy is spent creating this fast lane for charge transport, the magnitude of the wave decays, and *so does its velocity.* A similar process happens in streamer discharges. Please note that this is *different* than the transmission line interpretation of a lightning channel. In a transmission line, the amplitude of the wave decays as a function of distance due to the existence of a finite resistance. However, the wave velocity, which is a function of the inductance and capacitance only, remains constant – it does *not* decrease.

3.6 Systematic Error

There is an extreme amount of scattering in the source locations associated with the initial CGs (shown in dark blue in Figures 7 and 8). This is most likely caused by poor matching in this region as individual branches of the downward leader were well resolved by the INTF01 but not by the INTF02, because the flash started essentially directly overhead of the INTF01. The INTF01 antennas also have a null in their sensitivity at 90° overhead so there were gaps in the detected sources, and more work needs to be done to precisely measure the relative orientation of the two arrays.

It is not clear if the large dip in velocity around 7 km in Figure 13 is a real signal or simply a systematic error. There is no obvious increase in scattering of sources for any of the dart leaders or K leaders that pass through this region to indicate that the dip is caused by increasing location error, but it is suspicious that the dip occurs almost exactly along the baseline between the two INTF stations. Figure 16 highlights the location of the dip along the third CG dart leader by coloring points by velocity rather than the standard time coloring. The location of the velocity dip in Figure 16a can easily be identified as the channel color changes from yellow, to green, to blue, and back to yellow in a short period, which coincides with the point where the line between INTF01 and INTF02 crosses the channel. Location errors for the Triangulation method can be increased along this line as small changes in measured azimuth lead to large differences in the calculated range to the point, but this would be expected to manifest as a significant broadening of the channel along this line, which does not appear to be the case. The third dart leader is shown in the plot. As we previously pointed out, all 3 dart leaders and the K leader exhibiting this dip in speed have it at the same channel location.

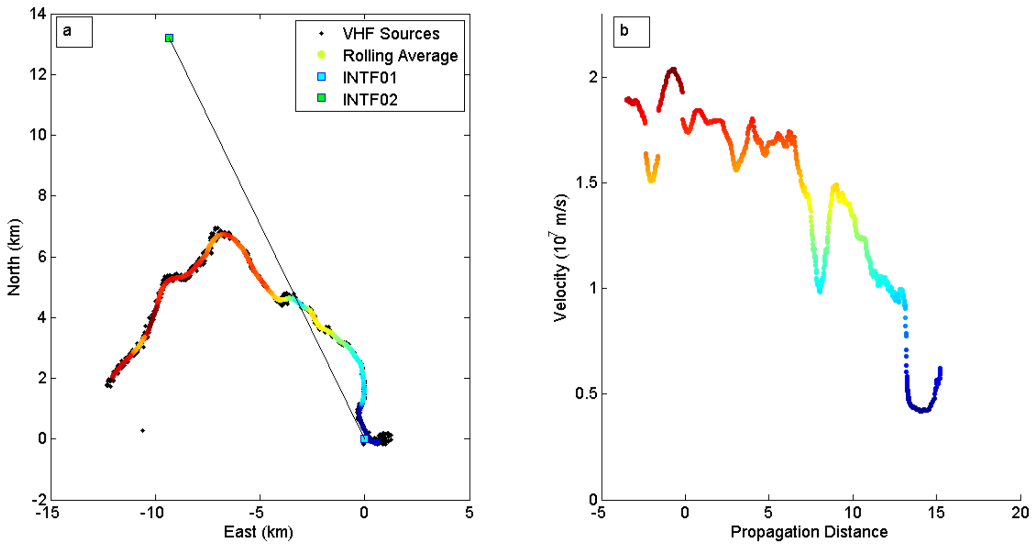

Figure 16. Plot showing the correspondence between the large dip in velocity at about 8 km along the channel and the baseline between the two INTF stations for the second dart leader. north/south and east/west location of sources and stations (a), and velocity vs propagation distance (b). Sources are colored by velocity.

4 Conclusions

In this paper we have:

Documented in an appendix a double theodolite location method for use in lightning interferometry. The original work contained a typographical error which left the algorithm ambiguous. We have also extended it to allow for interferometers of non-zero size (theodolites can be considered to be points!), and for arbitrary configurations of the two stations.

Verified the minimum accuracy of a 3DINTF Using a two station INTF colocated with a 7-station LMA, we showed that 3DINTF can have good location accuracy (200 m median error), and sufficient time-resolution to observe rapid processes like dart leaders and K leaders in detail. In checking the location accuracy of the INTF for sources located by both instruments, the LMA was assumed to be “correct”. In fact, for the 7-station LMA used, the LMA errors might also have been in the 100 m range.

Shown that charge identification can be done with an INTF The charge layers we identified were consistent with those found be an LMA, though less complete at this time. We speculate here that, because of the high spatial and temporal sample density of an INTF, future studies might allow one to observe the “granularity” of charges in a cloud (in other words, recognizing smaller charge pockets in addition to the overall layers in a storm.

Profiled in time and space the velocities of dart leaders and K leaders in the cloud INTF data rates allow measurement of faster phenomena like dart leaders, which could previously only be observed in detail using optical techniques below clouds.

Observed that leader velocity increases with “conditioning”. For all but the first K leader, the velocity generally increased with subsequent leaders on the same channel. The similar velocity of the last two dart leaders also suggests the channel may asymptotically approach a maximum level of "conditioning".

Noted that leader velocity decreases with channel progression. All dart and K leaders consistently showed 2X-3X velocity decreases as they progressed over 15-20 km. Because so much of these leaders were horizontal, this effect is likely not a pressure effect. We have weak evidence that it is not precisely an effect of storm-level electric field either. Our most likely conclusion is that the velocity decreases as available overvoltage at the channel tip decreases as energy is pumped into ionizing a lengthening column of air.

Observed a "slow lane" in the thunderstorm In addition to the general velocity decrease with channel progression our spatially resolved measurements saw a pair of dips in dart-leader propagation speed that were linked to particular locations in the storm.

Pointed out that dart and K leaders can be recognized in VHF images by relative lack of branching This result is apparent from high speed video. It is also apparent in INTF images as reported by Shao et al. (1995), that initial stepped leaders are much "fuzzier" than subsequent dart leaders. This "fuzz" is likely highly branched channels which are not reionized in the second pass of a dart leader. This would make sense if the over-voltage needed for reionization is lower because of a chemical conditioning process.

Appendix A Triangulation: The Double Theodolite Method

This algorithm is taken from(Thyer, 1962) and (Liu et al., 2018). It was decided to reproduce a large portion of their work as a service to the community because (Thyer, 1962) contains a typographical error, corrected here. New also herein is a generalization to arbitrary station locations and an allowance for the non-zero size of each interferometer. The algorithm determines the points of closest approach between the "line of sight" of the two stations (defined by their azimuth and elevation measurements). Figure A1 shows a diagram for the location process. The source location is chosen along the line between the points of closest approach. The point is weighted to be closer to the line of sight of the station that is closer to the source, to satisfy

$$\frac{DS}{SC} = \frac{AD}{BC} \tag{A1}$$

where AD is the distance between points A and D as shown in Figure A1, BC is the distance between points points B and C, DS is the distance between points D and S, and SC is the distance between points S and C.

For an INTF station with 3 antennas, the antennas form a plane. There is a line perpendicular to this plane where the relative time of arrival will be the same at all three antennas for any source on the line. The point where that line intersects the plane of the antennas is the circumcenter of the triangle defined by the antennas. The reported azimuth and elevation angles have an origin at the circumcenter. For the triangulation algorithm the circumcenter of each station is the location for the A and B points. For stations with more than 3 antennas there is not in general a well defined center. The azimuth and elevation measurements are also not well defined in general for more than 3 antennas since there is a different origin for every combination of 3 antennas. However, for an array that is small relative to the distance to the source, the difference in angle measured from the different origins may be smaller than the uncertainty in each angle measurement caused by other sources of error. Additional antennas are also useful if a least squares minimization method is applied after triangulation.

The double theodolite algorithm assumes that the second INTF station is directly north of the first. If this is not the case simply calculate the azimuth of the second

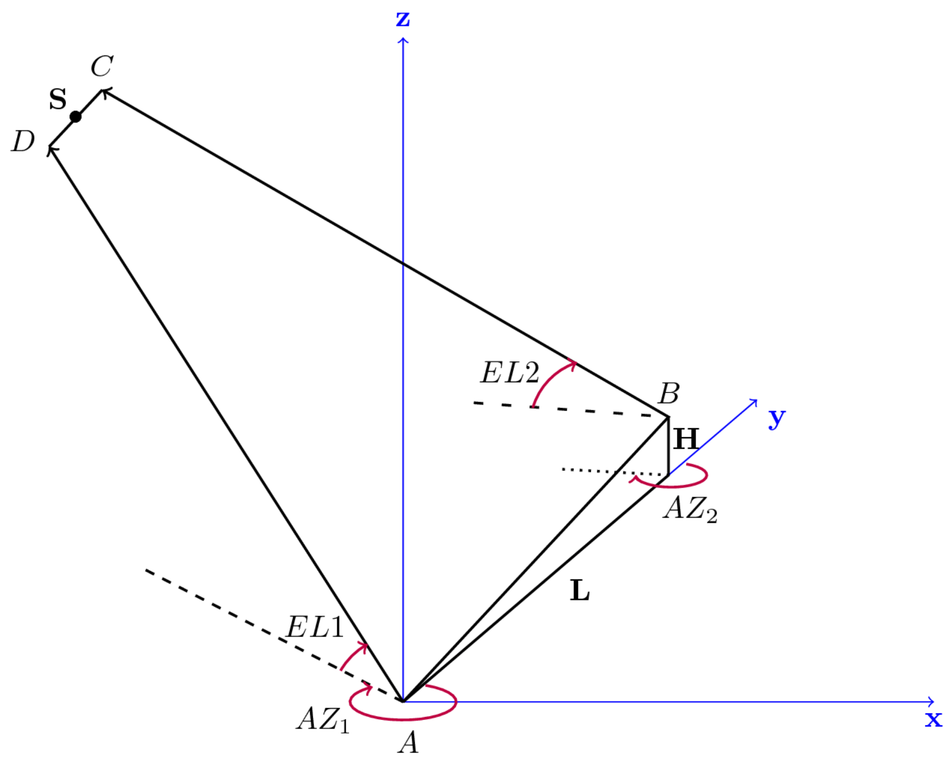

Figure A1. A diagram inspired by (Liu et al., 2018) for the double theodolite triangulation, showing station 1 (A), station 2 (B), their azimuth and elevation measurements (AZ1, EL1, and AZ2, EL2). Point D is the point of closest approach along the line of sight for station 1, and point C is the point of closest approach along the line of sight from station 2. Point S is the source location.

station relative to the first,

$$az_{1\rightarrow 2} = \tan^{-1}\left(\frac{B_x - A_x}{B_y - A_y}\right) \tag{A2}$$

where A_x and B_x are the east-west aligned x coordinates of station 1 and 2 respectively in linear units (meters, etc.), and A_y and B_y are the north-south aligned coordinates, and $az_{1\rightarrow 2}$ is the azimuthal direction of station 2 relative to station 1. The azimuth values for sources detected by each station should then be shifted as

$$AZ_{shifted} = AZ_{original} - az_{1\rightarrow 2} \tag{A3}$$

to align with the shifted coordinate system.

The VHF sources are projected onto a sphere of radius 1 (any units), with x (east), y (north), and z (altitude) coordinates of

$$x_1 = \cos(EL_1)\sin(AZ_1) \tag{A4}$$
$$y_1 = \cos(EL_1)\cos(AZ_1) \tag{A5}$$
$$z_1 = \sin(EL_1) \tag{A6}$$

where EL_1 is the elevation of the source measured from station 1, defined as the angle measured up from horizontal. AZ_1 is the azimuth angle of the source measured from station 1, with zero defined to be north and the angle increasing clockwise when down on a map view. Similarly we calculate

$$x_2 = \cos(EL_2)\sin(AZ_2) \tag{A7}$$
$$y_2 = \cos(EL_2)\cos(AZ_2) \tag{A8}$$
$$z_2 = \sin(EL_2) \tag{A9}$$

for the coordinates relative to station 2.

The line connecting the points of closest approach must be perpendicular to both of the lines of sight, so we calculate the cross product components

$$c_x = z_1 y_2 - y_1 z_2 \tag{A10}$$
$$c_y = x_1 z_2 - z_1 x_2 \tag{A11}$$
$$c_z = y_1 x_2 - x_1 y_2 \tag{A12}$$
$$|\vec{c}| = \sqrt{c_x^2 + c_y^2 + c_z^2} \tag{A13}$$

and the normalized cross product components

$$\hat{c}_x = c_x/|\vec{c}| \tag{A14}$$
$$\hat{c}_y = c_y/|\vec{c}| \tag{A15}$$
$$\hat{c}_z = c_z/|\vec{c}| \tag{A16}$$

We use the additional quantities of $L = \sqrt{(A_x - B_x)^2 + (A_y - B_y)^2}$ for the horizontal distance between the two stations and $H = B_z - A_z$ for the altitude difference between stations 2 and 1. L and H should be in the same linear units, their units will determine the units of the final calculated positions. We choose meters. We then calculate the range along the lines of sight to the points of closest approach as

$$R_1 = \frac{L(x_2\hat{c}_z - z_2\hat{c}_x) + H(\hat{c}_x y_2 - x_2\hat{c}_y)}{|\vec{c}|} \tag{A17}$$
$$R_2 = \frac{L(x_1\hat{c}_z - z_1\hat{c}_x) + H(\hat{c}_x y_1 - x_1\hat{c}_y)}{|\vec{c}|} \tag{A18}$$
$$R_3 = \frac{Lc_x + Hc_z}{|\vec{c}|} \tag{A19}$$

where R_1 is the distance between station 1 and the point of closest approach along station 1's line of sight, and R_2 is the distance between station 2 and the point of closest approach along station 2's line of sight, and R_3 is the length of the line between the two points of closest approach.

We then calculate the source position as

$$X' = R_1 x_1 + \frac{R_3 R_1}{R_1 + R_2}\hat{c}_x \tag{A20}$$

$$Y' = R_1 x_1 + \frac{R_3 R_1}{R_1 + R_2}\hat{c}_y \tag{A21}$$

$$Z' = R_1 x_1 + \frac{R_3 R_1}{R_1 + R_2}\hat{c}_z \tag{A22}$$

(A23)

where the X', Y', and Z' coordinates are relative to the location of station 1.

This source location can then be corrected for the coordinate shift that was needed to align the stations in the y direction, and the altitude can be set relative to sea level, so the final corrected source locations are

$$X = X'\cos(-az_{1\to2}) - Y'\sin(-az_{1\to2}) \tag{A24}$$

$$Y = X'\sin(-az_{1\to2}) + Y'\cos(-az_{1\to2}) \tag{A25}$$

$$Z = Z' + A_z \tag{A26}$$

where $az_{1\to2}$ is calculated in Equation A2. The X and Y coordinates are still relative to station 1, but it is convenient to have a local reference frame.

Acknowledgments

We thank Isaac Edelman for assistance with the double theodolite figure.

This work has been supported by the NSF EPSCoR Program under award OIA-1757207, by NSF award AGS-1917069, by Defense University Research Instrumentation Program award W911NF-16-1-0512, by collaborative grants from Vaisala and Earth Networks, by a Centennial Grant from the American Geophysical Union, and by the Australian-American Fulbright Foundation.

The field operations at Langmuir Laboratory were conducted on the Cibola National Forest under a Special Use Permit from the U.S. Forest Service.

All data supporting our conclusions is publicly available at `https://doi.org/10.5281/zenodo.4273188`. (License: Creative Commons Attribution 4.0 International, open access). (Jensen et al., 2020)

References

Akita, M., Nakamura, Y., Yoshida, S., Morimoto, T., Ushio, T., Kawasaki, Z., & Wang, D. (2010). What occurs in k process of cloud flashes? *Journal of Geophysical Research: Atmospheres*, *115*(D7). Retrieved from `https://agupubs.onlinelibrary.wiley.com/doi/abs/10.1029/2009JD012016` doi: 10.1029/2009JD012016

Bazelyan, E. M., & Raizer, Y. P. (1997). *Spark Discharge.* CRC Press.

Bazelyan, E. M., & Raizer, Y. P. (2000). *Lightning physics and lightning protection.* CRC Press.

Behnke, S. A., Thomas, R. J., Krehbiel, P. R., & Rison, W. (2005). Initial leader velocities during intracloud lightning: Possible evidence for a runaway breakdown effect. *Journal of Geophysical Research: Atmospheres*, *110*(D10). Retrieved from `https://agupubs.onlinelibrary.wiley.com/doi/abs/10.1029/2004JD005312` doi: 10.1029/2004JD005312

Bitzer, P. M., Christian, H. J., Stewart, M., Burchfield, J., Podgorny, S., Corredor, D., . . . Franklin, V. (2013). Characterization and applications of vlf/lf source locations fromlightning using the huntsville alabama marx meter array. *Journal of Geophysical Research: Atmospheres*, *118*(8), 3120-3138. Retrieved from `https://agupubs.onlinelibrary.wiley.com/doi/abs/10.1002/jgrd.50271` doi: 10.1002/jgrd.50271

Cummins, K. L., Krider, E. P., & Malone, M. D. (1998). The us national lightning detection network and applications of cloud-to-ground lightning data by electric power utilities. *IEEE Transactions on Electromagnetic Compatibility*, *40*(4), 465-480.

Ding, Z., Rakov, V. A., Zhu, Y., & Tran, M. D. (2020). On a possible mechanism of reactivation of decayed branches of negative stepped leaders. *Journal of Geophysical Research: Atmospheres*, *n/a*(n/a), e2020JD033305. Retrieved from `https://agupubs.onlinelibrary.wiley.com/doi/abs/10.1029/2020JD033305` (e2020JD033305 2020JD033305) doi: https://doi.org/10.1029/2020JD033305

Edens, H., Eack, K., Rison, W., & Hunyady, S. (2014). Photographic observations of streamers and steps in a cloud-to-air negative leader. *Geophysical Research Letters*, *41*(4), 1336–1342.

Edens, H. E., Eack, K. B., Eastvedt, E. M., Trueblood, J. J., Winn, W. P., Krehbiel, P. R., . . . Thomas, R. J. (2012). Vhf lightning mapping observations of a triggered lightning flash. *Geophysical Research Letters*, *39*(19). Retrieved from `https://agupubs.onlinelibrary.wiley.com/doi/abs/10.1029/2012GL053666` doi: https://doi.org/10.1029/2012GL053666

Hamlin, T., Krehbiel, P., Thomas, R., Rison, W., & Harlin, J. (2003). Electrical structure and storm severity inferred by 3-d lightning mapping observations during STEPS. In *Proc. 12th int. conf. on atmospheric electricity* (pp. 189–192).

Hare, B., Scholten, O., Dwyer, J., Ebert, U., Nijdam, S., Bonardii, A., . . . Winchen, T. (2020). Radio emission reveals inner meter-scale structure of negative lightning leader steps. *Phys. Rev. Lett.*, *124*.

Hare, B. M., Scholten, O., Bonardi, A., Buitink, S., Corstanje, A., Ebert, U., . . . Winchen, T. (2018). Lofar lightning imaging: Mapping lightning with nanosecond precision. *Journal of Geophysical Research: Atmospheres*, *123*(5), 2861-2876. Retrieved from `https://agupubs.onlinelibrary.wiley.com/doi/abs/10.1002/2017JD028132` doi: 10.1002/2017JD028132

Hayenga, C. O. (1984). Characteristics of lightning vhf radiation near the time of return strokes. *Journal of Geophysical Research: Atmospheres*, *89*(D1), 1403-1410. Retrieved from `https://agupubs.onlinelibrary.wiley.com/doi/abs/10.1029/JD089iD01p01403` doi: 10.1029/JD089iD01p01403

Jensen, D., Sonnenfeld, R., Stanley, M., Edens, H., da Silva, C., & Krehbiel, P. (2020, November). *Supplementary Material for: Dart Leader and K Leader Velocity From Initiation Site to Termination Time-Resolved with 3D Interferometry.* Zenodo. Retrieved from `https://doi.org/10.5281/zenodo.4273188` doi: 10.5281/zenodo.4273188

Jordan, D. M., Idone, V. P., Rakov, V. A., Uman, M. A., Beasley, W. H., & Jurenka, H. (1992). Observed dart leader speed in natural and triggered lightning. *Journal of Geophysical Research: Atmospheres*, *97*(D9), 9951-9957. Retrieved from `https://agupubs.onlinelibrary.wiley.com/doi/abs/10.1029/92JD00566` doi: 10.1029/92JD00566

Karunarathna, N., Marshall, T. C., Karunarathne, S., & Stolzenburg, M. (2017). Initiation locations of lightning flashes relative to radar reflectivity in four small florida thunderstorms. *Journal of Geophysical Research: Atmospheres*, *122*(12), 6565-6591. doi: 10.1002/2017JD026566

Kawasaki, Z., Mardiana, R., & Ushio, T. (2000). Broadband and narrowband rf interferometers for lightning observations. *Geophysical Research Letters*, *27*(19), 3189-3192. Retrieved from https://agupubs.onlinelibrary.wiley.com/doi/abs/10.1029/1999GL011058 doi: 10.1029/1999GL011058

Kitagawa, N. (1957). On the mechanism of cloud flash and junction or final process in flash to ground. *Papers in Meteorology and Geophysics*, *7*(4), 415-424. doi: 10.2467/mripapers1950.7.4_415

Krehbiel, P. R. (1986). The electrical structure of thunderstorms. In *The earth's electrical environment* (pp. 90–113). Washington, D.C.: National Academy Press.

Liu, H., Qiu, S., & Dong, W. (2018). The three-dimensional locating of vhf broadband lightning interferometers. *Atmosphere*, *9*(8), 317.

Loeb, L. B. (1966). The mechanisms of stepped and dart leaders in cloud-to-ground lightning strokes. *Journal of Geophysical Research (1896-1977)*, *71*(20), 4711-4721. Retrieved from https://agupubs.onlinelibrary.wiley.com/doi/abs/10.1029/JZ071i020p04711 doi: 10.1029/JZ071i020p04711

Mardiana, R., Kawasaki, Z.-I., & Morimoto, T. (2002). Three-dimensional lightning observations of cloud-to-ground flashes using broadband interferometers. *Journal of Atmospheric and Solar-Terrestrial Physics*, *64*(1), 91 - 103. Retrieved from http://www.sciencedirect.com/science/article/pii/S1364682601000992 doi: https://doi.org/10.1016/S1364-6826(01)00099-2

Marshall, T. C., Stolzenburg, M., Maggio, C. R., Coleman, L. M., Krehbiel, P. R., Hamlin, T., ... Rison, W. (2005). Observed electric fields associated with lightning initiation. *Geophysical Research Letters*, *32*(3). Retrieved from https://agupubs.onlinelibrary.wiley.com/doi/abs/10.1029/2004GL021802 doi: https://doi.org/10.1029/2004GL021802

Mazur, V. (2016). The physical concept of recoil leader formation. *Journal of Electrostatics*, *82*, 79–87.

Oetzel, G. N., & Pierce, E. T. (1969). Vhf technique for locating lightning. *Radio Science*, *4*(3), 199-202. Retrieved from https://agupubs.onlinelibrary.wiley.com/doi/abs/10.1029/RS004i003p00199 doi: 10.1029/RS004i003p00199

Poehler, H., & Lennon, C. L. (1979). Lightning detection and ranging system ldar system description and performance objectives. *NASA Technical Report*. Retrieved from https://ntrs.nasa.gov/search.jsp?R=19790025501

Proctor, D. E. (1971). A hyperbolic system for obtaining vhf radio pictures of lightning. *Journal of Geophysical Research (1896-1977)*, *76*(6), 1478-1489. Retrieved from https://agupubs.onlinelibrary.wiley.com/doi/abs/10.1029/JC076i006p01478 doi: 10.1029/JC076i006p01478

Rakov, V. A. (1998). Some inferences on the propagation mechanisms of dart leaders and return strokes. *Journal of Geophysical Research: Atmospheres*, *103*(D2), 1879-1887. Retrieved from https://agupubs.onlinelibrary.wiley.com/doi/abs/10.1029/97JD03116 doi: 10.1029/97JD03116

Rhodes, C. T., Shao, X. M., Krehbiel, P. R., Thomas, R. J., & Hayenga, C. O. (1994). Observations of lightning phenomena using radio interferometry. *Journal of Geophysical Research: Atmospheres*, *99*(D6), 13059-13082. Retrieved from https://agupubs.onlinelibrary.wiley.com/doi/abs/10.1029/94JD00318 doi: 10.1029/94JD00318

Rison, W., Thomas, R. J., Krehbiel, P. R., Hamlin, T., & Harlin, J. (1999). A gps-based three-dimensional lightning mapping system: Initial observations in central new mexico. *Geophysical Research Letters*, *26*(23), 3573-3576. Retrieved from https://agupubs.onlinelibrary.wiley.com/doi/abs/10.1029/1999GL010856 doi: 10.1029/1999GL010856

Schonland, B. F. J., Malan, D. J., Collens, H., & Boys, C. V. (1935). Progressive lightning ii. *Proceedings of the Royal Society of London. Series A - Mathematical and Physical Sciences*, *152*(877), 595-625. Retrieved from https://royalsocietypublishing.org/doi/abs/10.1098/rspa.1935.0210 doi: 10.1098/rspa.1935.0210

Shao, X. M., Holden, D. N., & Rhodes, C. T. (1996). Broad band radio interferometry for lightning observations. *Geophysical Research Letters*, *23*(15), 1917-1920. Retrieved from https://agupubs.onlinelibrary.wiley.com/doi/abs/10.1029/96GL00474 doi: 10.1029/96GL00474

Shao, X. M., & Krehbiel, P. R. (1996). The spatial and temporal development of intracloud lightning. *Journal of Geophysical Research: Atmospheres*, *101*(D21), 26641-26668. Retrieved from https://agupubs.onlinelibrary.wiley.com/doi/abs/10.1029/96JD01803 doi: 10.1029/96JD01803

Shao, X. M., Krehbiel, P. R., Thomas, R. J., & Rison, W. (1995). Radio interferometric observations of cloud-to-ground lightning phenomena in florida. *Journal of Geophysical Research: Atmospheres*, *100*(D2), 2749-2783. Retrieved from https://agupubs.onlinelibrary.wiley.com/doi/abs/10.1029/94JD01943 doi: 10.1029/94JD01943

Stock, M. (2014). *Broadband interferometry of lightning.* New Mexico Institute of Mining and Technology.

Stock, M., Akita, M., Krehbiel, P., Rison, W., Edens, H., Kawasaki, Z., & Stanley, M. (2014). Continuous broadband digital interferometry of lightning using a generalized cross-correlation algorithm. *Journal of Geophysical Research: Atmospheres*, *119*(6), 3134–3165.

Thomas, R. J., Krehbiel, P. R., Rison, W., Hamlin, T., Boccippio, D. J., Goodman, S. J., & Christian, H. J. (2000). Comparison of ground-based 3-dimensional lightning mapping observations with satellite-based LIS observations in Oklahoma. *Geophys. Res. Lett.*, *27*(12), 1703–1706.

Thomas, R. J., Krehbiel, P. R., Rison, W., Hunyady, S. J., Winn, W. P., Hamlin, T., & Harlin, J. (2004). Accuracy of the lightning mapping array. *Journal of Geophysical Research: Atmospheres*, *109*(D14). Retrieved from https://agupubs.onlinelibrary.wiley.com/doi/abs/10.1029/2004JD004549 doi: 10.1029/2004JD004549

Thyer, N. (1962). Double theodolite pibal evaluation by computer. *Journal of applied meteorology*, *1*(1), 66–68.

Warwick, J. W., Hayenga, C. O., & Brosnahan, J. W. (1979). Interferometric directions of lightning sources at 34 mhz. *Journal of Geophysical Research: Oceans*, *84*(C5), 2457-2468. Retrieved from https://agupubs.onlinelibrary.wiley.com/doi/abs/10.1029/JC084iC05p02457 doi: 10.1029/JC084iC05p02457

Williams, E. R. (1989). The tripole structure of thunderstorms. *Journal of Geophysical Research: Atmospheres*, *94*(D11), 13151-13167. Retrieved from https://agupubs.onlinelibrary.wiley.com/doi/abs/10.1029/JD094iD11p13151 doi: 10.1029/JD094iD11p13151

Winn, W. P. (1965). A laboratory analog to the dart leader and return stroke of lightning. *Journal of Geophysical Research (1896-1977)*, *70*(14), 3265-3270. Retrieved from https://agupubs.onlinelibrary.wiley.com/doi/abs/10.1029/JZ070i014p03265 doi: 10.1029/JZ070i014p03265

Winn, W. P., Aulich, G. D., Hunyady, S. J., Eack, K. B., Edens, H. E., Krehbiel, P. R., … Sonnenfeld, R. G. (2011). Lightning leader stepping, k changes, and other observations near an intracloud flash. *Journal of Geophysical Research: Atmospheres*, *116*(D23). Retrieved from https://agupubs.onlinelibrary.wiley.com/doi/abs/10.1029/2011JD015998 doi: 10.1029/2011JD015998

Wu, T., Wang, D., & Takagi, N. (2018). Lightning mapping with an array of fast antennas. *Geophysical Research Letters*, *45*(8), 3698-3705. Retrieved from https://agupubs.onlinelibrary.wiley.com/doi/abs/10.1002/2018GL077628 doi: 10.1002/2018GL077628